CRYSTAL GROWTH & DESIGN

pubs.acs.org/crystal

Article

Hydrothermal Synthesis and Catalytic Assessment of High-Silica (B,Fe)-beta Zeolites

Published as part of a Crystal Growth and Design virtual special issue on Zeolite Crystal Engineering

Alessia Marino, Enrico Catizzone,* Massimo Migliori, Giorgia Ferrarelli, Alfredo Aloise, Donatella Chillè, Georgia Papanikolaou, Paola Lanzafame, Siglinda Perathoner, Gabriele Centi, and Girolamo Giordano

Cite This: *Cryst. Growth Des.* 2023, 23, 2988–3001

Read Online

ACCESS | Metrics & More | Article Recommendations

ABSTRACT: The synthesis of high-silica BEA zeolite has attracted great attention from the zeolite scientific community, and several approaches have been proposed for the preparation of crystalline materials with a very low aluminum content. In this work, high-silica crystalline BEA zeolites were prepared starting from an Al-free synthesis gel, by using boron and iron as trivalent atoms. A Si/Fe molar ratio equal to 100, 200 or ∞ was adopted, and crystallization was successful in the presence of tetraethylammonium (TEA^+), with a low Si/B starting synthesis gel molar ratio, i.e. 8 or 12, and with a hydrothermal synthesis time of 6 days maximum at 150 °C. The Si/Fe ratio affects TEA^+−zeolite interactions, crystallographic patterns, and surface acidity. In particular, the proposed synthesis procedure allowed obtaining BEA zeolites with a very low acidity, with a tunable Lewis/Brønsted acids site distribution. Liquid-phase etherification of 5-hydroxymethyl furfural (HMF) with ethanol highlighted the suitability of the obtained materials for the production of 5-(ethoxymethyl)furan-2-carbaldeyde (EMF), a green fuel additive. Particularly, a high EMF selectivity (>97%) was obtained in the presence of both iron and boron. As the main outcome, the presented results indicated that high-silica BEA zeolite can be easily obtained starting from a low Si/B ratio in the synthesis gel, with conventional tetraethylammonium as a template, and iron can be also incorporated for catalytic purposes.

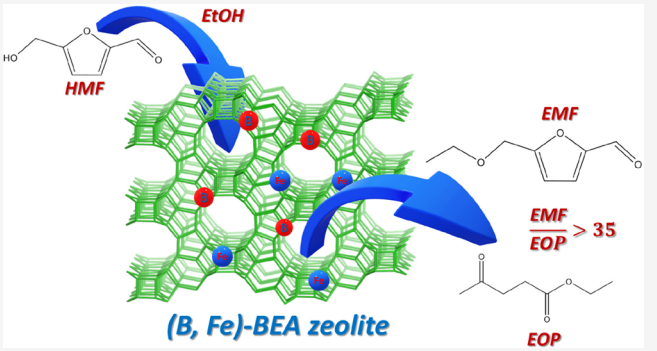

1. INTRODUCTION

Zeolites are crystalline microporous materials that find several applications on an industrial scale, such as adsorption, ion exchange, and, particularly, heterogeneous catalysis.[1−3] The presence of molecular-sized pores allows the control of selectivity control toward a preferred transition state and/or products. The use of zeolites in specific applications strongly depends on several factors such as zeolite structure (i.e., openings, shape and orientation of the channels), chemical composition, acidity, and crystal size and morphology,[4−9] and this is a key point especially for catalysis.

Zeolites can be both natural and synthetic materials. The publication of the preparation procedure of the first synthetic zeolite dates back to 1862, when St.Claire-Deville reported the hydrothermal synthesis of levinite, *the first example of the synthesis in laboratory of a natural zeolite.*[10] During the mid-twentieth century, there was a tremendous growth of studies devoted to the synthesis of zeolites, mainly focused on the replication of the natural structures. The revolution in the field occurred with the preparation of a synthetic zeolite structure without any corresponding natural material. In this regard, beta zeolite was the first pure synthetic zeolite with a high silica composition, with the Si/Al ratio ranging from 5 to 100, prepared using an organic template (tetraethylammonium, TEA^+).[11] After that, aiming to obtain tailored materials, there was strong scientific and industrial development in the synthesis of zeolites with new structures and characteristics, driven by the characteristics of the specific process these materials were supposed to be used in. Currently, few zeolite structures have found significant catalytic application in petrochemical and refining industries, as most of the 240 known zeolite framework types are characterized by either high synthesis costs or lack of performance improvements with respect to the implemented technologies. Examples of

Received: January 25, 2023
Revised: February 27, 2023
Published: March 7, 2023

industrial processes that use zeolites as catalysts are fluidized catalytic cracking (FCC) with USY, hydroisomerization and dewaxing with SAPO-11, ZSM-5, or SSZ-32, light paraffin isomerization with mordenite, xylene isomerization and toluene alkylation with ZSM-5, the methanol-to-olefins process with SAPO-34, and cumene production with beta zeolite.[12,13]

The beta structure consists of a three-dimensional network of channels (12-membered-ring openings) with diameters of 7.6 × 6.4 and 5.5 × 5.5 Å. The maximum diameter of the sphere that can be included into the beta voids is 6.68 Å and this characteristic classifies beta as a large-structure zeolite. Beta zeolite is also considered a disordered zeolite structure, as it may consist of intergrowing networks of two or three different polymorphs: namely, Beta_A, Beta_B, and Beta_C. Several techniques have been developed to tune the amount of each polymorph, and several studies on the effect of synthesis gel composition and crystallization conditions on beta zeolite characteristics have been reported.[14−16] Beta zeolite was first synthesized in 1967 by Wadlinger et al.[11] by adopting a basic synthesis gel containing TEA^+ as template. The authors were able to synthesize aluminum-containing beta zeolite with a wide range of Si/Al molar ratios, i.e. 5−100; worldwide, the synthesis of beta zeolite with Si/Al in the range of 10−30 is common and easily implementable. In contrast , the synthesis of beta crystals with a Si/Al ratio out of this range is more difficult to achieve and innovative strategies have to be adopted to reach this target. For instance, specific crystallization conditions are requested for beta zeolite with a very high aluminum content per tetragonal unit cell with high crystallinity degree. As an example, Borade and Clearfield[17] prepared an aluminum-rich beta zeolite (Si/Al = 5.2, corresponding to 10.3 aluminum atoms per tetragonal unit cell) by adopting a relatively dense synthesis gel with a $TEAOH/Al_2O_3$ ratio of 1.7, lower than the commonly used ratio (around $TEAOH/Al_2O_3$ = 27.5). Dealumination is also a technique commonly adopted to obtain high-silica beta, usually carried out via leaching with mineral acids or high-temperature steaming, although this postsynthesis treatment generates mesopores and crystalline loss.[18−21] As an example, Salagre[22] et al. prepared beta zeolite with Si/Al > 100 by acid-assisted dealumination of commercial beta zeolite (Si/Al = 10) also using a microwave treatment, with a significant crystallinity loss.

On the other hand, the direct synthesis of beta zeolite at a very high Si/Al molar ratio requires unconventional methods, since the addition of a heteroatom (such as aluminum) seems to be unavoidable to promote the nucleation step of crystallization.

Bregolato et al.[23] used 4,4′-trimethylenebis(*N*-benzyl-*N*-methyl-piperidinium) dihydroxide, $TMP(OH)_2$, as a special template to prepare beta crystals with Si/Al > 500, which were applied as catalysts for the methylation of phenol. van Bekkum et al.[24] prepared boron-containing beta zeolite with a Si/B molar ratio from 20 to infinite by using dibenzyldimethylammonium as a template, also adding high-silica beta seeds. Moreover, the synthesis of high-silica beta using a "conventional" organic structure directing agent, such as TEA^+, is still a relevant issue. In this regard, Corma et al.[25] reported the synthesis of all-silica beta zeolite by using TEA^+, but in the presence of fluorine ions. The mechanism of crystallization was also investigated by Serrano and co-workers.[26]

Mintova published several studies on the preparation and the application of high-silica beta zeolite.[27−31] For instance, Mintova and co-workers prepared pure silica nanoscale beta zeolite with a monomodal crystal size distribution with a mean size of about 100 nm starting from a colloidal precursor by using the TEA^+ ion as a template and freshly freeze-dried colloidal silica, and they used the materials obtained to prepare uniform films via spin-coating.[27] They also reported that, by increasing the aluminum content in the synthesis gel, the crystallization rate of nanosized beta zeolite increases. As an example, the crystallization time needed to be prolonged from 72 to 264 h, by increasing Si/Al from 32 to infinity in the synthesis gel.[28] In addition, in another paper, Mintova and co-workers studied the effect of the silica source, i.e. TEOS or Cab-O-Sil, OSDA type, i.e. $TPM(OH)_2$ or TEAOH, and heating method, i.e. conventional or microwave oven, on the properties of high-silica beta zeolite, with interesting results in terms of the crystal size and stability of the obtained suspension.[29]

Furthermore, the control of aluminum content and the possibility to carry out isomorphic substitution with other trivalent atoms (such as Fe, B, Ge, and Ga) are considered suitable strategies to modulate the acidity of such zeolites, especially for applications in which acid site strength plays a crucial role, as in catalysis.[32−36] Also in this field, several approaches have been proposed.

Taramasso et al.[37] published the first paper on the synthesis on boron-containing beta zeolite, by adopting an alkali-free synthesis gel and by using TEA^+ as a structure-directing agent.

Kallus et al.[38] reported the synthesis of boron-containing beta through an almost neutral fluoride aqueous gel using 1,4-diazabicyclo[2.2.2]octane and methylamine as a template, indicating that the boron-silicate network formation probably occurs through condensation of boron and silicon fluorides and hydroxyl-fluoride ions. de Ruiter et al.[39] proposed the phase diagram of beta synthesis in the presence of boron and aluminum and TEAOH as a template, indicating that particular conditions have to be adopted in order to prevent the formation of competitive phases, such as MTW and MOR.

Furthermore, also the preparation of iron-containing zeolites has attracted great attention,[40] and in this regard, ZSM-5 is the most studied zeolite for iron incorporation, while the preparation of iron-containing beta has been less extensively studied, although the beta structure is an attractive host for iron atoms, especially when it is applied in catalysis.[41−44]

To the best of our knowledge, no studies have been reported on the preparation of Al-free beta zeolite starting from a synthesis gel containing both boron and iron.

In this study, we report the synthesis and characterization of (B,Fe)-beta zeolites prepared with different Si/Fe molar ratios in the synthesis gel (namely 100, 200, and infinite), by adopting procedures mostly similar to those used to obtain conventional Al-Beta, especially in terms of crystallization time and SDA type (TEA^+). The objective of the paper is to study the effect of synthesis gel composition on the surface properties, e.g. acidity, and on the catalytic performances in the etherification of 5-hydroxymethyl furfural (HMF) with ethanol.

HMF is a biomass-derived platform molecule that can be used for the production of green chemicals, playing a role of bridge between biomass and the biorefinery industry.[45−47] The HMF etherification reaction has an applicative interest in the production of green fuel additives,[48] and it is strongly dependent on acid site types and strength, as reported in our previous papers.[49,50] In particular, in this study we focused on

https://doi.org/10.1021/acs.cgd.3c00085
Cryst. Growth Des. 2023, 23, 2988−3001

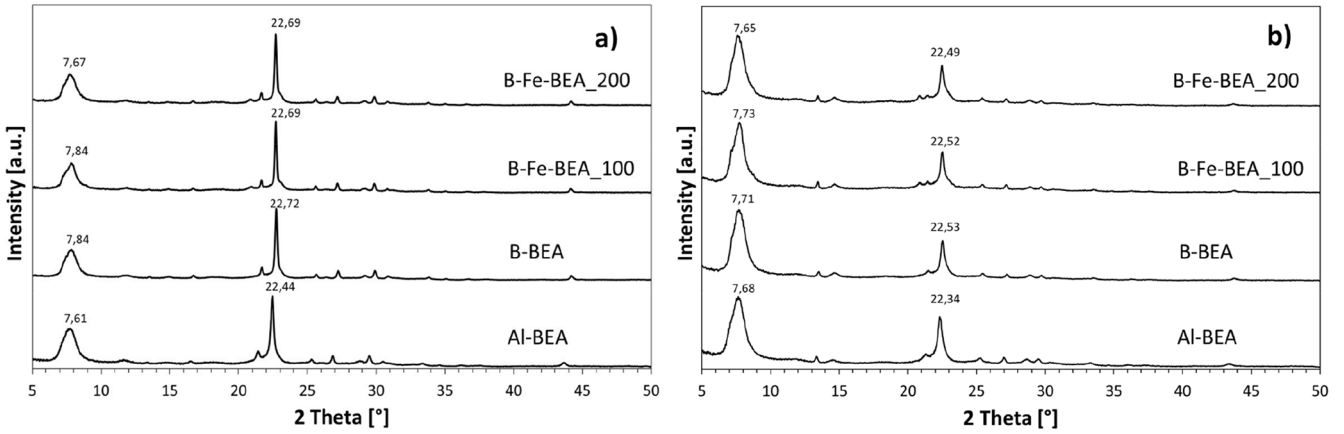

Figure 1. XRD patterns of as-synthesized (a) and H-form (b) materials.

the formation of 5-(ethoxymethyl)furan-2-carbaldeyde (EMF). The etherification of HMF can be considered a suitable probe reaction to investigate the role of surface properties of the prepared Al-free (B,Fe)-beta zeolite samples.

2. EXPERIMENTAL SECTION

2.1. Sample Preparation. The BEA sample (Si/Al_{gel} = 25) used as reference was prepared using the procedure published elsewhere[51] and starting from a synthesis gel with the molar ratio 1 SiO_2−0.02 Al_2O_3−0.10 Na_2O−0.20 TEAOH−10 H_2O.

The reaction was carried out by using precipitated silica gel (SiO_2 100%, Merck), Tetraethylammonium hydroxide (TEAOH 40%, Sigma-Aldrich) as a structure-directing agent (SDA), sodium aluminate ($NaAlO_2$ 98%, Sigma-Aldrich), sodium hydroxide (NaOH 97%, Carlo Erba Reagenti), and ultrapure water.

The gel was stirred at room temperature for 2 h and then transferred to a Teflon-lined stainless-steel autoclave and kept at 150 °C for 6 days. After cooling, the solid was recovered by filtration, washed with distilled water, and dried at 105 °C overnight. The sample was calcined at 550 °C for 8 h at a heating rate of 5 °C/min in a tubular oven, under static air, for the organic template removal. This procedure leads to a beta zeolite with Si/Al_{bulk} = 38.

The synthesis of boron-containing beta (labeled as B-BEA) was carried out by modifying the previously described procedure, from the synthesis gel 1 SiO_2−0.12 H_3BO_3−0.06 Na_2O−0.20TEAOH-10 H_2O.

The reaction was performed by using boric acid (H_3BO_3 100%, Riedel-de Haen). The crystallization parameters were set at 6 days and 150 °C; afterward, the sample was recovered and calcined under an N_2 flow (30 mL/min, 5 °C/min up to 550 °C, holding time 1 h) and then under an air flow (15 mL/min, holding time 7 h) to remove the SDA.

The syntheses of B-Fe-BEA zeolites were carried out by using the synthesis gel composition 1 SiO_2−0.08H_3BO_3−0.05 Na_2O−0.20 TEAOH−10 H_2O−$x$$Fe_2O_3$.

The stochiometric coefficient of iron (x) was varied to obtain Si/Fe ratios equal to 100 and 200: i.e., x = 0.005 and 0.0025, respectively.

An aqueous solution of iron nitrate ($Fe(NO_3)_3$·$9H_2O$ 98%, Sigma-Aldrich) and oxalic acid ($H_2C_2O_4$·$2H_2O$ 99.8%, Analyticals) was prepared and then added to an aqueous solution containing NaOH, TEAOH, and H_3BO_3. Finally, silica was slowly added. The final suspension was stirred at room temperature for 2 h and then transferred to the autoclave and heated at 150 °C. The crystallization time was dependent upon the x value (6 days for x = 0.005, 5 days for x = 0.0025). Lastly, the SDA was removed by calcination at 550 °C for 8 h under static air at a heating rate of 5 °C/min.

All prepared catalysts underwent through the same activation procedure, which involved two cycles of ionic exchange with NH_4Cl (1 M, at 80 °C per 2 h each), followed by calcination at 550 °C for 8 h at a heating rate of 5 °C/min to obtain the acidic form.

2.2. Sample Characterization. The crystallinity and purity of synthesized phases were evaluated by X-ray powder diffraction (XRD) spectroscopy in the 5° < 2θ < 50° region, with a step size of 0.02° s^{-1} and X-ray wavelength of 1.5406 Å (Rigaku Miniflex 600).

TG/DTA profiles of as-synthesized samples were acquired by a TA Instruments SDT 650 device. Each sample was heated to 850 °C, at a heating rate of 5 °C/min under an air flow (100 mL/min).

The chemical composition of the final solid was obtained by means of the atomic absorption technique with a GBC 932AA instrument.

The particle morphology of the samples was examined using a Quanta 200 (FEI) scanning electron microscope (SEM).

The surface area was determined via nitrogen adsorption isotherms at −196 °C (ASAP 2020 Micromeritics) and applying the BET (Brunauer−Emmett−Teller) method to estimate the surface area. The t-plot method was utilized to calculate the external area and micropore volume. The samples were outgassed at 300 °C for 1 h to remove impurities prior to the measurement.

Surface acidity was measured via both NH_3-TPD and FT-IR analysis. For NH_3-TPD measurements about 100 mg of the sample was loaded in a linear quartz microreactor and pretreated at 300 °C under a helium flow for 1 h to remove adsorbed water. The sample was cooled to 150 °C and saturated with a 10% (vol) NH_3/He mixture at a flow rate of 20 STP mL min^{-1} for 2 h. Ammonia that was physically adsorbed was removed by purging in helium at 150 °C for 1 h until TCD baseline stabilization. Desorption measurements were carried out in the temperature range of 100−550 °C (10 °C min^{-1}) using a helium flow rate of 20 STP mL min^{-1}. Peak analysis and deconvolution was performed by using commercial software (PeakFit 4.12, Seasolve-USA).

FT-IR measurements were performed using a Nicolet iS 10 instrument (Thermo Scientific, USA), equipped with a DTGS detector. The samples were first compressed (pressure 2.65 t cm^{-2}) into a wafer of about 25 mg and pretreated at 400 °C under vacuum (about 10^{-5} Torr). FT-IR spectra were recorded under vacuum at room temperature to characterize the silanol groups in the zeolite materials. To obtain more information about Brønsted and Lewis acidity, the adsorption of probe molecules was performed using d_3-acetonitrile and pyridine. The adsorption of d_3-acetonitrile was carried out at room temperature by exposing samples wafers to probe vapors with subsequent evacuation for 1 h at the same temperature prior to vacuum FTIR spectral acquisition.[52,53] The adsorption of pyridine was carried out at room temperature by exposing sample wafers to probe vapor pressure. The physisorbed pyridine was removed from the sample at 150 °C and 10^{-5} Torr for 60 min before spectrum acquisition. The Lambert−Beer law was used to evaluate the total number of acid sites, starting from the integrated area of the bands of the protonated species through the equation $A = \varepsilon N \rho$, where A is the area of bands obtained from the spectra, ε is the molar extinction coefficient (cm $mmol^{-1}$), N is the concentration of the vibrating species (mmol g^{-1}), and ρ is the density of the sample wafer (mass/

https://doi.org/10.1021/acs.cgd.3c00085
Cryst. Growth Des. 2023, 23, 2988−3001

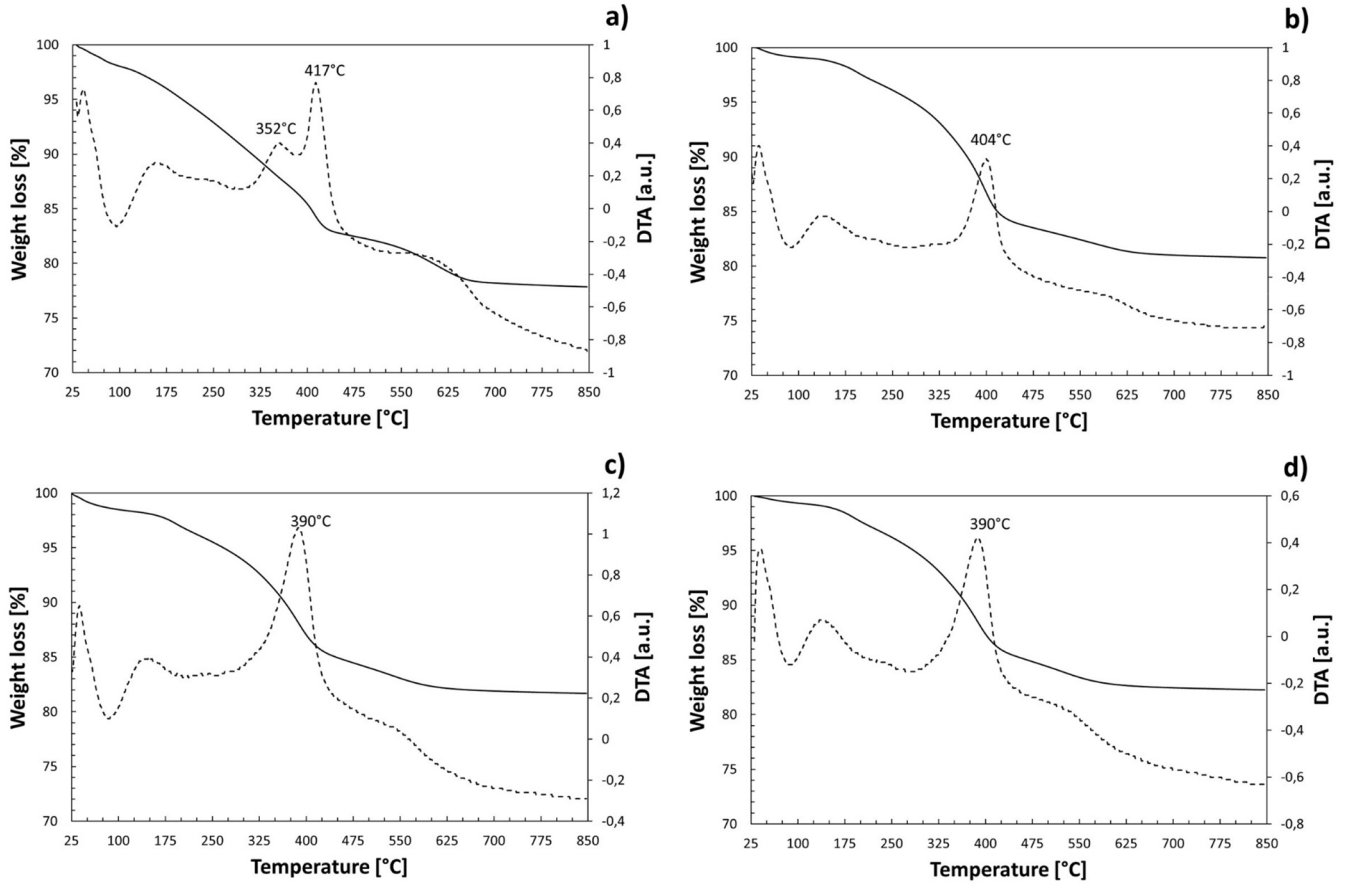

Figure 2. TGA (continuous line) and DTA (dashed line) profiles of (a) Al-BEA, (b) B-BEA, (c) B-Fe-BEA_100, and (d) B-Fe-BEA_200.

area ratio of the pellet, mg cm^{-2}). The values of the molar extinction coefficients used were ε = 2.05 cm μmol^{-1} for d_3-acetonitrile interacting with Brønsted acid sites (band at ca. 2297 cm^{-1}), ε = 3.6 cm μmol^{-1} for d_3-acetonitrile interacting with Lewis sites (band at 2310−2325 cm^{-1}), and ε = 0.74 cm μmol^{-1} for d_3-acetonitrile interacting with silanols (band at 2275 cm^{-1}).[54] For the pyridine probe, the concentration of the Brønsted and Lewis acid sites was calculated via integration of the peaks at 1545 and 1445 cm^{-1}, using 2.2 and 1.67 cm μmol^{-1} as the molar extinction coefficient, respectively.[49] FT-IR spectra presented were all normalized with respect to the disk density.

2.3. Catalytic Tests. The catalytic etherification of HME to EMF was carried out in batch mode. In a typical HMF etherification reaction experiment, 0.1 g of catalyst, 2.5 mmol of HMF, and 3.5 mL of ethanol were placed in a Teflon-lined autoclave. The reaction was carried out at 140 °C under autogenic pressure, and EMF formation was monitored by sampling at 1, 3, and 5 h and quantification by using an Agilent 7890A-GC-FID instrument equipped with a Rxi-5 ms capillary column (length 30 m, diameter 0.25 mm, and film thickness 0.25 μm) using pure compounds for calibration curves. Before sampling and quantification, the reactor was quenched in an ice-containing bath, and the reaction mixture was separated from the catalyst by filtration.

3. RESULTS AND DISCUSSION

3.1. Physicochemical properties. The XRD pattern of beta samples before and after activation in protonic form are reported in Figure 1. The obtained XRD has characteristic reflections of BEA topology. In particular, two main peaks at 7.64−7.84 and 22.44−22.72° are observed together with other minor peaks typical of a beta structure. No hump in the 2θ region 20−30° due to amorphous material is observed, while a trace of impurities at 2θ = 20.83−20.88° is observed for iron-containing samples. Probably, such a peak can be assigned to the MTW phase, which is very competitive with the beta phase.[39]

As a reference, XRD of the home-synthesized BEA zeolite with Si/Al equal to 25 is also reported. In the case of as-synthesized materials, in the range 20−30°, the main diffraction peak of the Al-containing sample (Al-BEA) is centered at 22.44°, while that of the B-containing Fe-free sample (B-BEA) and that of B−Fe-containing sample (B-Fe-BEA_100 and B-Fe-BEA_200) are centered at 22.72 and 22.69°, respectively, as a consequence of the difference in terms of solid composition. Furthermore, it is interesting to note that in all the B-containing samples a shoulder appears at the low-angle side in the first low-angle diffraction peak, indicating that these materials are nearer to polymorph A than to polymorph B.[25]

By considering the area of the main diffraction peak centered in the range 22−23°, the as-synthesized B-BEA sample exhibited the highest crystallinity, which was taken as a reference for the calculation of the relative crystallinity of the other B-Fe samples. In particular, a relative crystallinity equal to 87% is calculated for B-Fe-BEA_200, while a value of 75% is obtained for B−Fe_BEA_100 and Al-BEA, indicating that a high concentration of iron or aluminum is not beneficial in terms of crystallinity. After activation, a slight shift to lower angles is observed for all of the investigated samples, and the diffraction peak centered at 7−8° becomes the most intense. Furthermore, a different trend in terms of relative crystallinity is also observed. In particular, the H^+-form Al-BEA sample

https://doi.org/10.1021/acs.cgd.3c00085
Cryst. Growth Des. 2023, 23, 2988−3001

Table 1. Chemical Composition of the Investigated Samples

sample	Si/B_{gel} (mol/mol)	Si/B_{solid} (mol/mol)	B content in the solid (μmol/g)	Si/Fe_{gel} (mol/mol)	Si/Fe_{solid} (mol/mol)	Fe content in the solid (μmol/g)
B-BEA	8.3	118	140			
B-Fe-BEA_100	12.5	157	104	100	92	179
B-Fe-BEA_200	12.5	184	90	200	188	88

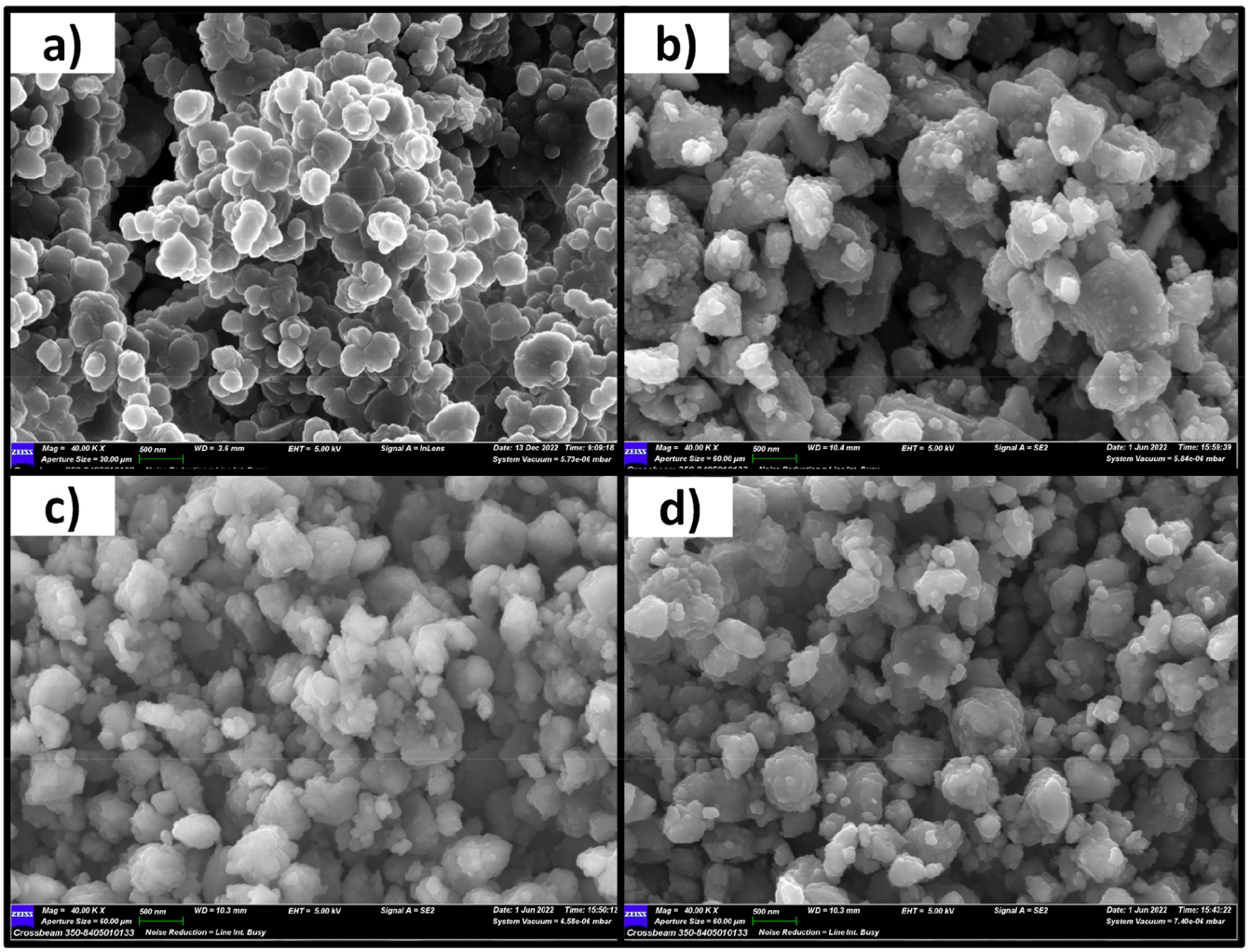

Figure 3. SEM images of (a) Al-BEA, (b) B-BEA, (c) B-Fe-BEA_100, and (d) B-Fe-BEA_200. Scale bar: 500 nm.

exhibits the highest crystallinity, followed by B-BEA (relative crystallinity 81%), B-Fe-BEA_200 (relative crystallinity 77%), and B-Fe-BEA_100 (relative crystallinity 65%). The drop in crystallinity of B-containing samples indicates that boron is probably expelled from the zeolite structure during activation, with a partial zeolite collapse, and this effect is more pronounced in the copresence of iron. The loss of crystallinity upon calcination is typical of boron-containing zeolites.[39]

The isomorphous substitution of Al with boron and/or iron has also a significant effect on template−zeolite interactions, as revealed in the TGA/DTA profiles of as-synthesized samples carried out under an air flow depicted in Figure 2.

The TGA curves show that there are distinct stages of weight losses, with an effect of the heteroatom type on the combustion peak temperature. The weight loss below 200 °C can be associated with the adsorbed water release from the zeolite surface. A higher amount of adsorbed water is measured for the Al-BEA sample (2.8% w/w), followed by B-Fe-BEA (1.8% w/w) and B-BEA (1.3% w/w) samples. This result indicates that the synthesized samples exhibit different levels of hydrophobicity, probably related to a different content of hydroxyl groups. Significant differences are also clearly observable in terms of combustion behavior. Several studies have been carried out on the thermal desorption/decomposition of TEA^+ species from BEA voids, indicating that usually there are two types of TEA^+ species: namely, occluded TEAOH molecules and TEA^+ species interacting with the zeolite framework. The latter play the role of charge-compensating cations of zeolite negative charges, and usually they are removed at higher temperature.[55,56] In particular, Pérez-Pariente and co-workers[56] determined distinct zones of weight loss during TGA of Al-containing beta zeolite: in the range 25−220 °C a slightly endothermic step was observed resulting from the water desorption, while at higher temperature, the weight loss was associated with the combustion of TEAOH species occluded in the zeolites in the range 220−350

https://doi.org/10.1021/acs.cgd.3c00085
Cryst. Growth Des. 2023, 23, 2988−3001

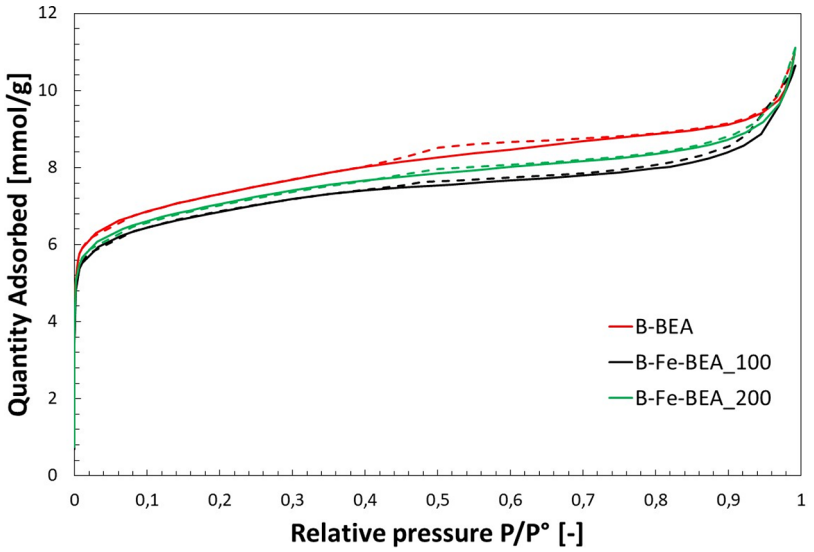

Figure 4. N_2 adsorption (continuous line) and desorption (dashed line) isotherms of the investigated high-silica samples.

°C, with the combustion of TEA^+ that acts as framework cations in the range 350−500 °C, and with the combustion of residual organic materials occluded in the zeolite pores.

DTA profiles of conventional Al-BEA zeolite with Si/Al = 25 exhibit three main combustion peaks centered at 352, 417, and about 600 °C. Therefore, the weight loss at lower temperature can be associated with the desorption/decomposition of TEAOH molecules occluded in the BEA voids, while the weight loss at higher temperature can be associated with a TEA^+ interaction with the framework aluminum negative charge. A completely different profile is observed for Al-free B- and B-Fe-containing samples. In particular, the main peak at about 404 °C is observed for the B-BEA sample, indicating the presence of TEA^+ interacting with zeolite negative charges probably associated with framework boron atoms. The lower combustion temperature of these species in B-BEA in withrespect to Al-BEA can be associated with the weaker TEA^+−framework bonds in the case of the B-containing framework. When iron is added, as in the case of the B-Fe-BEA sample, the main combustion peak is centered at about 390 °C, indicating that also iron contributes to stabilize TEA^+ species. The weight loss observed in the temperature range 220−850 °C was 16.2% for Al-BEA, 16.1% for B-BEA, and about 14.7% for both B-Fe-BEA_100 and B-Fe-BEA_200 samples. These results clearly indicate that a lower amount of template is incorporated in the case of iron-containing samples, while no significant differences are observed between Al- and B-containing samples.

Chemical analyses of calcined samples are reported in Table 1.

The Si/Fe molar ratio of the final solid is well in agreement with the Si/Fe ratioadopted in the synthesis gel, indicating that all of the iron is incorporated in the zeolite. In contrast, the measured Si/B molar ratio in the solid is significantly higher that the Si/B molar ratio in the synthesis gel, revealing that stable boron incorporation is very difficult to obtain. Furthermore, the iron content in the zeolite does not seem affect the boron content. In fact, by increasing the iron content from 88 to 179 μmol/g, a similar boron content (90−104 μmol/g) is obtained. Therefore, the obtained iron-containing materials can be considered as solids with rather similar boron contents and with very different iron contents.

The crystal morphology of the investigated samples was observed by means of scanning electronic microscopy, and acquired images are reported in Figure 3.

All the samples are composed of submicrometer crystals with a flattened spheroid shape. The Al-BEA sample mainly consists of crystals with a size of 250−300 nm, with the rare presence of crystals smaller than 100 nm. Al-free samples appear as particles of about 500 nm with also the presence of crystals smaller than this size. Similar results in the presence of boron were obtained by Derewinski and co-workers.[57]

The N_2 adsorption−desorption isotherms at 77 K of the investigated high-silica samples are reported in Figure 4.

The obtained N_2 isotherms are typical of microporous materials with a well-defined structure, typical of zeolites. A slight hysteresis is observed at high P/P° values, indicating some external mesoporosity, probably related to the presence of agglomerates of nanocrystals as observed by SEM analysis. The nitrogen uptake in the low P/P° range is higher for the B-BEA sample. In particular, the amounts of adsorbed nitrogen in the monolayer estimated by the BET method in the P/P° range 0.05−0.20 are equal to 5.8 mmol/g for B-BEA, 5.4 mmol/g for B-Fe-BEA_100, and 5.5 mmol/g for B-Fe-BEA_200. Globally, all three high-silica samples possess similar textural properties, in terms of BET area, external area, micropore area, and micropore volume, as reported in Table 2.

Table 2. Textural Properties of the Investigated Samples

sample	area BET (m^2/g)	external surface area (m^2/g)	micropore area (m^2/g)	micropore volume (cm^3/g)
Al-BEA	588	222	366	0.170
B-BEA	569	216	353	0.159
B-Fe-BEA_100	526	193	333	0.152
B-Fe-BEA_200	540	206	335	0.154

A slightly higher micropore area and volume are observed for the B-BEA sample. In agreement with XRD results, also textural properties confirm that the B-BEA sample exhibits the highest crystallinity among the investigated B-containing samples.

https://doi.org/10.1021/acs.cgd.3c00085
Cryst. Growth Des. 2023, 23, 2988−3001

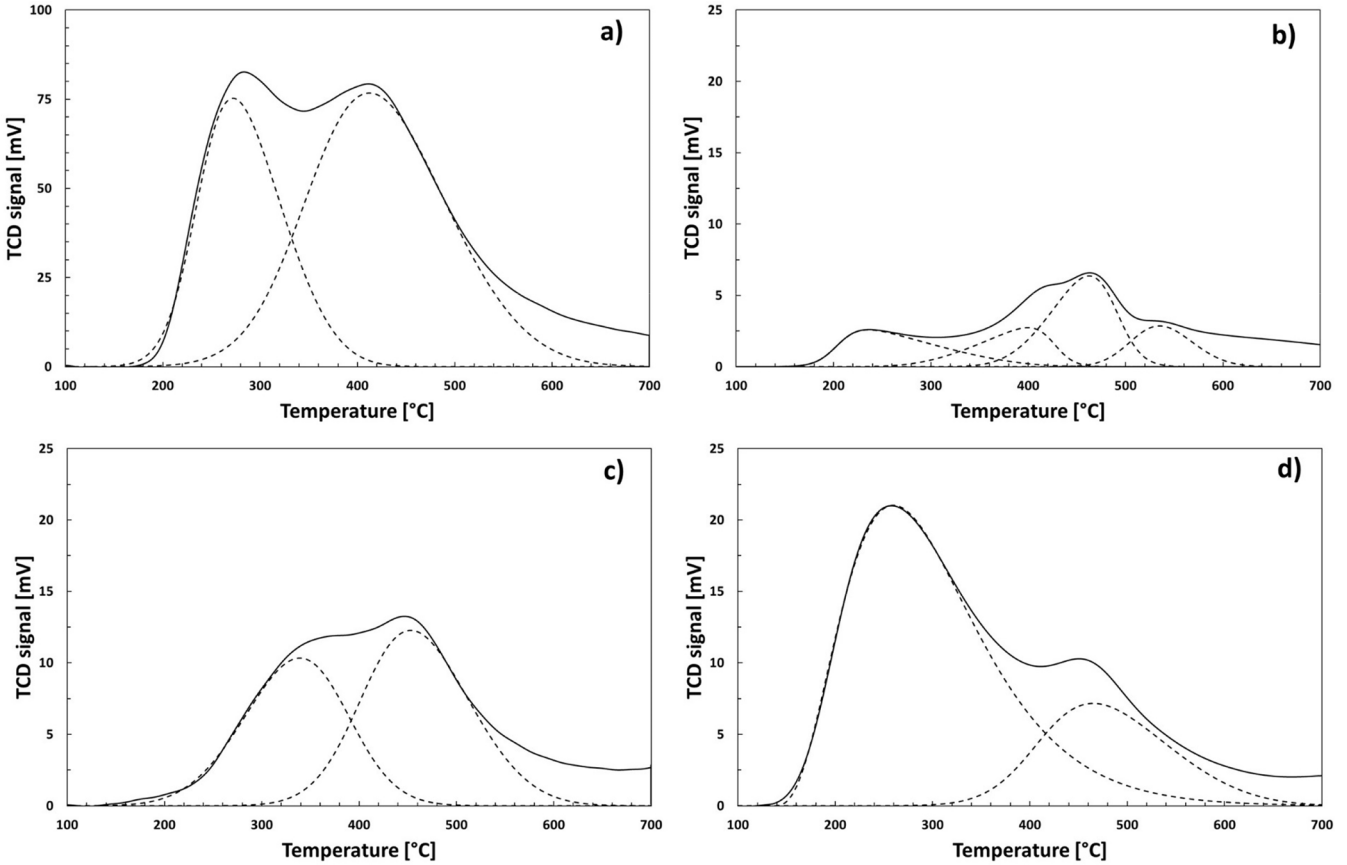

Figure 5. NH_3-TPD profiles (continuous lines) and deconvoluted curves (dashed lines) of (a) Al-BEA, (b) B-BEA, (c) B-Fe-BEA_100, and (d) B-Fe-BEA_200. Please note that the scale of the *y* axis of Al-BEA is 0−100 mW and that of B-containing samples is 0−25 mV.

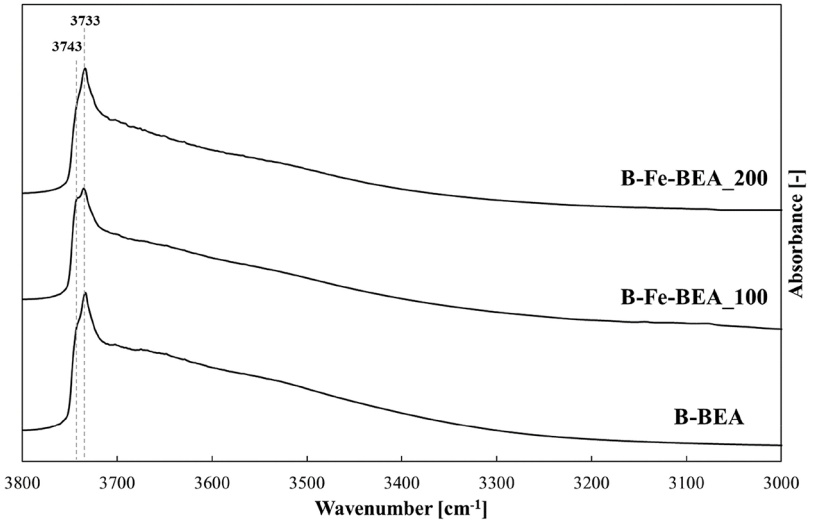

Figure 6. FT-IR spectra of samples activated at 400 °C under vacuum.

3.1.1. Acidity. Because of the low amount of trivalent atoms, the investigated samples are classified as high-silica zeolites, and a very low acidity is expected as a consequence. Therefore, in order to investigate their acidic features, both NH_3-TPD and FTIR techniques were adopted.

NH_3-TPD profiles are reported in Figure 5. As a reference, the NH_3-TPD profile of conventional Al-BEA with Si/Al = 25 is also reported. The profile of the Al-BEA sample consists of two well-defined bands, centered at 275 and 414 °C, respectively, indicating the presence of two families of NH_3−zeolite interactions. The lower-temperature band is usually associated with ammonia molecules adsorbed on ammonium ions, this being formed by means of the interaction between and ammonia and Brønsted acid sites.[58] As more than one ammonia molecule can interact with each ammonium ion, the lower-temperature band is not reliable for acidity estimation. In contrast, a second high-temperature band can be adopted for the estimation of the concentration of acid sites in the solid.

https://doi.org/10.1021/acs.cgd.3c00085
Cryst. Growth Des. 2023, 23, 2988−3001

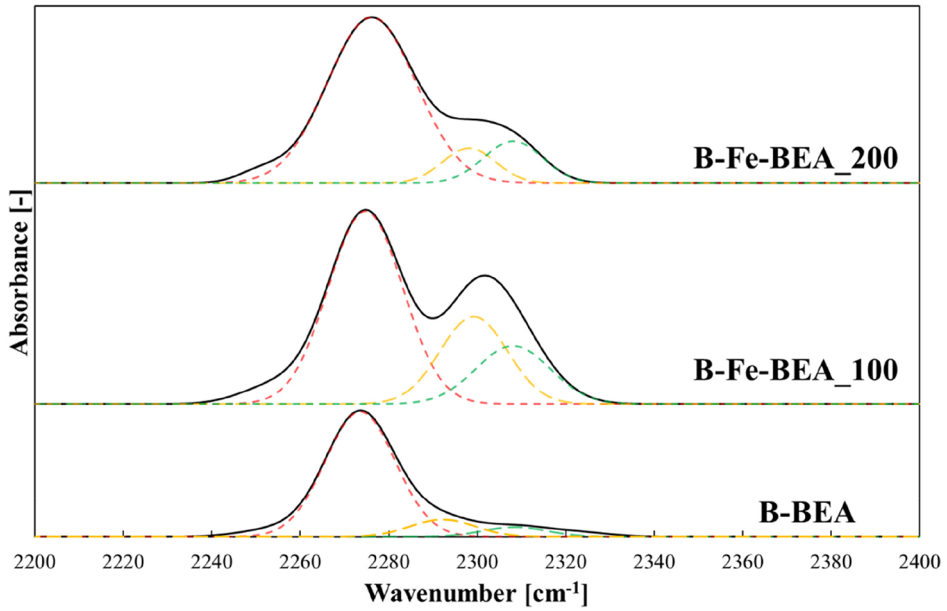

Figure 7. FT-IR spectra of d_3-acetonitrile adsorption on samples after evacuation at room temperature.

Furthermore, the TCD signal observed at a temperature higher than 600 °C can be reasonably assigned to water formed by silanol condensation.[59] In this regard, an acid site concentration of about 500 μmol/g is calculated for the Al-BEA sample. This value well matches with Si/Al_{bulk} = 38, corresponding to about 1.7 mol of Al per unit cell and, therefore, to about 450 $\mu mol_{Al}/g$. All the investigated B-containing samples exhibit an NH_3 uptake significantly lower than that of the conventional Al-BEA sample, with also some differences in terms of ammonia evolution profile. The B-BEA sample shows three main bands in the high-temperature region, centered at 400, 464, and 540 °C, indicating the presence of a wide inhomogeneous distribution of acid site strength, with an NH_3 uptake equal to 38 μmol/g. This value is significantly lower than the boron content measured by chemical analysis (see Table 1), i.e. 140 $\mu mol_B/g$, suggesting that only a part of the boron acts as an acid site that can be titrated by ammonia. When iron is also present in the zeolite, the NH_3 evolution profile has a main band centered at 460 °C for both B-Fe-BEA_100 and B-Fe-BEA_200 samples. The amount of adsorbed ammonia associated with this band is a function of iron content, as it equals 63 and 44 μmol/g for B-Fe-BEA_100 and B-Fe-BEA_200, respectively. Also in that case, the amount of titrated acid sites is significantly lower than the heteroatom content (see Table 1), indicating that a part of the iron is not acidic or leads to acid sites with a very low strength not titratable by ammonia. Globally, the NH_3-TPD results indicate that the investigated B-containing samples possess a very mild acidity, in terms of both amount and strength of acid sites.

Therefore, in order to better investigate the acidity of these samples, FT-IR measurements were also carried out.

Figure 6 shows the spectra of the samples in the OH-stretching region (3800−3000 cm^{-1}) obtained after a pretreatment at 400 °C without probe adsorption. Two characteristic bands have been identified for all samples: a band at about 3743 cm^{-1} related to isolated silanol groups located on the external surface and a band at about 3733 cm^{-1} linked to the presence of isolated silanol groups sited in the micropores.[53] Both B-BEA and B-Fe-BEA_200 sample spectra revealed an evident peak at 3733 cm^{-1}, while the band at 3743 cm^{-1} consisted of a unpronounced shoulder. The intensity of the band related to the quantity of hydroxyl species present in the samples demonstrated that internal isolated silanol groups were more abundant than silanol groups at the external surface. For B-Fe-BEA_100, the intensity of the external silanol band at 3743 cm^{-1} increased, although the peak at 3733 cm^{-1} remained the highest. No evident bands typical of bridging Brønsted acid sites at a lower wavenumber value,[60] e.g. around 3600 cm^{-1}, were observed, due to the low content of both B and Fe.

Figure 7 compares IR spectra of samples interacting with d_3-acetonitrile (2200−2400 cm^{-1}).

The results obtained showed the presence of three characteristic bands: the first band at about 2275 cm^{-1} was related to the interaction of the probe with terminal silanols located in the internal area and external surface of the zeolites, the second band at about 2290 cm^{-1} indicated a d_3-acetonitrile interaction with Brønsted acid sites, and the third band at about 2320 cm^{-1} was associated with Lewis acid sites. In Table 3 numerical quantification of d_3-acetonitrile uptake, obtained using molar extinction coefficients, is summarized.

Table 3. Acid Site Distribution of the Catalysts Obtained by CD_3CN FT-IR Measurements

	d_3-acetonitrile uptake (μmol/g)		
band position and assignment	B-BEA	B-Fe-BEA_100	B-Fe-BEA_200
Lewis sites (2320 cm^{-1})	11	50	22
Brønsted sites (2290 cm^{-1})	14	89	28
silanols (2275 cm^{-1})	313	633	534

Considering all the samples, the B-BEA sample exhibited the lowest amount of Brønsted and Lewis acid sites and of silanols that can be titrated by d_3-acetonitrile. In contrast, the presence of iron increased the amount of titrated acid sites. Particularly, the B-Fe-BEA_100 zeolite, with the highest iron content, exhibited the highest amount of d_3-acetonitrile uptake on

https://doi.org/10.1021/acs.cgd.3c00085
Cryst. Growth Des. 2023, 23, 2988−3001

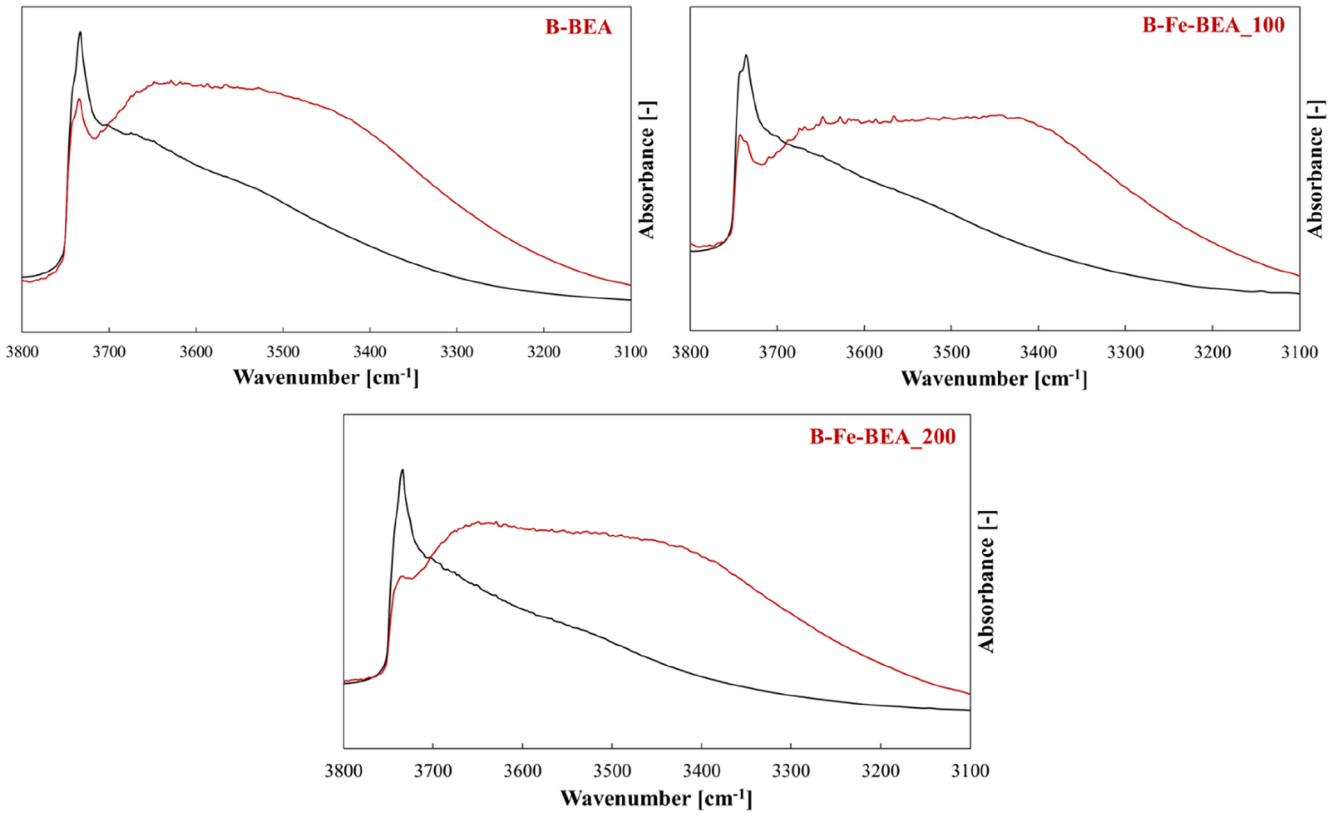

Figure 8. FT-IR spectra in the OH region (3800−3100 cm^{-1}) before (black lines) and after evacuation of adsorbed d_3-acetonitrile (red lines).

Brønsted, Lewis, and silanol sites, indicating a higher acidity with respect to the other samples. Furthermore, in the case of iron-containing samples, the iron content seems to affect preferably the amount of Brønsted and Lewis sites interacting with d_3-acetonitrile, with a less significant effect on silanol amount. In fact, by increasing the iron amount from 88 μmol/g to 179 μmol/g the Brønsted + Lewis acid sites titrated by d_3-acetonitrile increases from 50 to 139 μmol/g, while the silanol content interacting with the probe only slightly decreases from 633 to 534 μmol/g. Moreover, the presence of iron leads to obtain more highly defective samples. As observed during NH_3-TPD measurements, a very low acidity is observed for boron-containing iron-free samples, i.e. B-BEA, indicating that most of the boron present in the sample, about 140 μmol/g, leads neither to Brønsted nor to Lewis acidity.

Figure 8 shows sample spectra obtained before and after d_3-acetonitrile adsorption (after outgassing at 150 °C for 1 h).

As can be seen, adsorption of d_3-acetonitrile caused a strong reduction of hydroxyl bands as result of the interaction of the probe with both internal and external silanols. Important evidence was obtained from the spectra of B-Fe-BEA_100 after the absorption of d_3-acetonitrile. In fact, the band of internal silanols at about 3733 cm^{-1} decreased more than the band of external silanols at 3743 cm^{-1}. This result demonstrated that external silanol groups of the sample are weaker than the internal groups and interact less with this small probe. Moreover, for all samples, spectra recorded after d_3-acetonitrile adsorption exhibited a new very broad band at lower frequency which can be related to the silanol groups interacting with probe vapor.[61]

Figure 9 shows the FT-IR spectra of the samples in the range commonly used to identify Lewis and Brønsted acid sites interacting with pyridine (1700−1400 cm^{-1}).

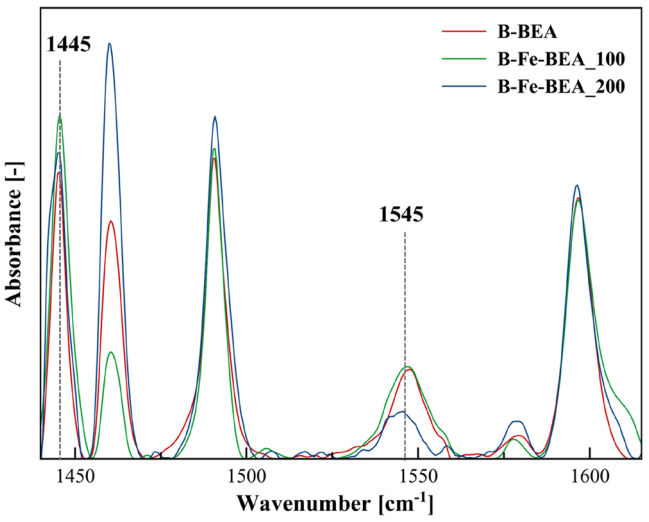

Figure 9. FT-IR spectra of pyridine adsorption on samples after evacuation at 150 °C under vacuum.

The spectra were acquired at room temperature, after vacuum evacuation at 150 °C for 1 h in order to eliminate the contribution of physiosorbed pyridine. Among others, two bands were identified and studied: that at 1445 cm^{-1} is attributed to the Lewis acid sites, and the other at 1545 cm^{-1} is related to the Brønsted acid sites, both bonded to pyridine. Through the deconvolution of the mentioned peaks, using the

https://doi.org/10.1021/acs.cgd.3c00085
Cryst. Growth Des. 2023, 23, 2988−3001

extinction coefficients, the micromoles of pyridine adsorbed on the Lewis and Brønsted acid sites of the samples were quantified. The results are summarized in Table 4. B-Fe-

Table 4. Brønsted and Lewis Acid Site Distribution of the Catalysts Obtained by Pyridine FT-IR Measurements

	pyridine uptake (μmol/g)		
band position and assignment	B-BEA	B-Fe-BEA_100	B-Fe-BEA_200
Lewis sites (1445 cm^{-1})	53	79	50
Bronsted sites (1545 cm^{-1})	49	65	29

BEA_100 exhibited the highest amount of Brønsted and Lewis acid sites. In particular, as an effect of the iron insertion into the structure of B-Fe-BEA_100, Lewis acid sites increased by about 50% compared to the B-BEA sample while Brønsted acid sites increased by 35%. The same trend was not found for B-Fe-BEA_200 probably due to the relatively low iron content in the synthesis gel and to the lower B amount with respect to the B-BEA sample. The results obtained showed that there are differences between the acid sites titrated by pyridine and those titrated by d_3-acetonitrile. The fact that pyridine is also able to titrate weak Lewis sites while d_3-acetonitrile only interacts with strong Lewis acid sites is a reliable explanation for the quantified differences from the two adsorbed probes.[50] Moreover, the most significant differences between pyridine and d_3-acetonitrile titration are observed for the B-BEA sample. In particular, the total probe molecule uptake on Brønsted + Lewis sites of B-BEA increases from 25 μmol/g in the case of d_3-acetonitrile to 102 μmol/g in the case of pyridine (+308%). In contrast, comparing d_3-acetonitrile to pyridine, the total probe molecule uptake increases from 139 to 144 μmol/g (+4%) in the case of B-Fe-BEA_100 and from 50 to 79 μmol/g (+60%) in the case of B-Fe-BEA_200, suggesting that B-BEA samples exhibit a much weaker acidity than iron-containing samples. This result indicates that boron has a much weaker acidity than iron. Therefore, the insertion of both boron and iron could be a suitable strategy to obtain materials with a tailored acidity.

In order to refine the study of the probe adsorption on the synthesized samples, FT-IR spectra were acquired, in the range 3800−3100 cm^{-1}, after the following different procedures:

- before the pyridine adsorption (No_Py_Ads)
- after the probe adsorption and outgassing at room temperature (Out_Room_T)
- after the probe adsorption and outgassing at 150 °C (Out_150 °C).

The spectra are reported in Figure 10 (labels identify the test conditions) for all the investigated samples. Almost all the terminal silanols still interact, albeit weakly, with the pyridine, after 1 h of degassing at room temperature. In fact, the two bands at 3733 and 3743 cm^{-1} are significantly reduced in comparison with those of the samples degassed without probe. Moreover, after pyridine adsorption, the onset of a new interaction band at about 3665 cm^{-1} was observed. Furthermore, referring to the strength of the internal and external terminal silanol groups, other interesting evidence was

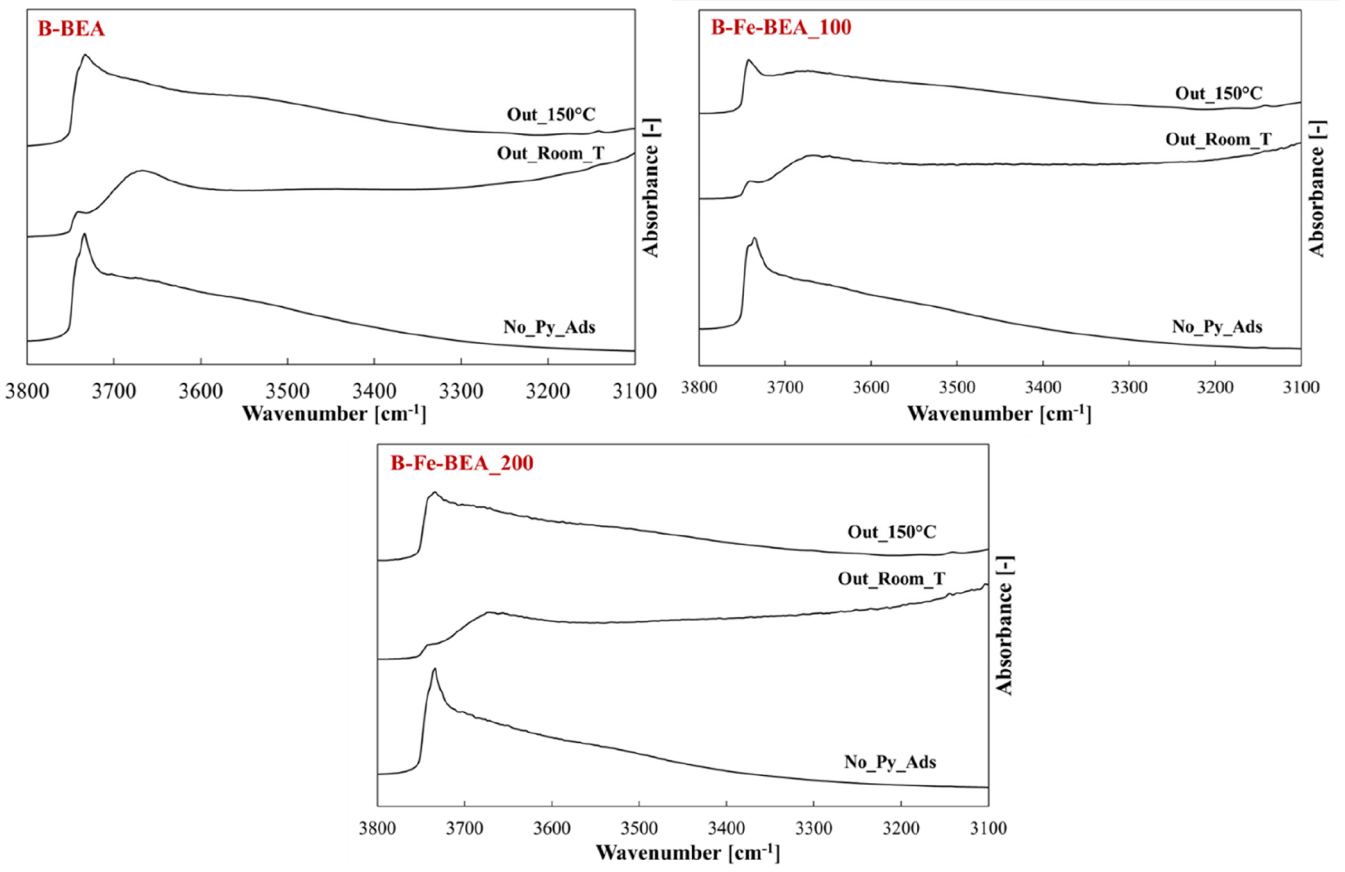

Figure 10. FT-IR spectra in the OH region (3800−3100 cm^{-1}) before pyridine adsorption (No_Py_Ads), after pyridine adsorption and outgassing at room temperature (Out_Room_T), and after pyridine adsorption and outgassing at 150 °C (Out_150 °C).

https://doi.org/10.1021/acs.cgd.3c00085
Cryst. Growth Des. 2023, 23, 2988−3001

obtained. In fact, related to the internal and external terminal silanols, respectively, the bands at 3733 and 3743 cm^{-1} again became evident and defined when the probe outgassing temperature was increased to 150 °C. This demonstrated that most terminal silanols were weakly bound to pyridine and the probe interaction was extinguished when samples were outgassed at a temperature higher than room temperature. However, a part of the terminal silanol groups continued to interact with pyridine. This evidence proved the highest strength of the portion of terminal silanols which are bound to pyridine even after 150 °C outgassing.

3.2. Catalytic Assessment of HMF Etherification. The synthesized boron- and iron-containing high-silica beta zeolites were tested in the etherification of HMF with ethanol, focusing on the formation of two key products: i.e., 5-(ethoxymethyl)-furan-2-carbaldehyde (EMF) and ethyl-oxo-pentanoate (EOP). The formation of such molecules strongly depends on the acidic properties of the catalyst. In fact, previous works demonstrated that Lewis acid sites are particularly selective toward the formation of EMF, while the presence of Brønsted acid sites promotex the conversion of both HMF and EMF into EOP.[62] Table 5 reports the catalytic performances of the investigated high-silica BEA zeolites. As reported in Figure 11, the HMF conversion follows the total acidity trend, being highest for the most acidic sample (B-Fe-BEA_100), which exhibits a HMF conversion equal to 87%, while conversions of 80% and 72% are observed for B-Fe-BEA_100 and B-BEA, respectively. As a comparison, previous results concerning the catalytic behavior of conventional Al-BEA with Si/Al = 25 are also reported.[63] In particular, conventional Al-BEA exhibits a HMF conversion equal to 95%, as a consequence of the high acid site concentration due to the high aluminum content.

Table 5. Catalytic Results during HMF Etherification with Ethanol[a]

sample	HMF conversion (%)	EMF yield (mmol/(h g))	EOP yield (mmol/(h g))
B-BEA	72	2.43	0.10
B-Fe-BEA_100	87	4.64	0.13
B-Fe-BEA_200	80	3.02	0.08
Al-BEA[b]	95	7.03	1.47

[a]Reaction conditions: initial concentration of HMF, 0.7 M; catalyst amount, 0.1 g; reaction temperature, 140 °C; reaction time, 3 h. [b]Reference 63.

When product yield is considered, the EMF yield follows the trend

$$\text{Al-BEA} > > \text{B-Fe-BEA\_100} > \text{B-Fe-BEA\_200} > \text{B-BEA}$$

while the EOP yield follows a different trend, i.e.

$$\text{Al-BEA} > > \text{B-Fe-BEA\_100} > \text{B-BEA} > \text{B-BEF} > \text{B-Fe-BEA\_200}$$

As mentioned above, the product selectivity is strongly affected by acid site type. As a rule, the presence of a higher concentration of Brønsted acid sites, as in the case of the Al-BEA sample, causes a lower selectivity toward EMF, as EOP formation is catalyzed by this type of acid site. Data reported in Figure 12 indicate the effect of Lewis-to-Brønsted acid sites on the EMF-to-EOP yield ratio. These results clearly indicate that the presence of iron is beneficial to EMF formation. The presence of iron allows obtaining high-silica BEA-type materials with a suitable Brønsted/Lewis acid site distribution and strength for the formation of EMF. In fact, by considering the acidity calculated from pyridine adsorption in FT-IR, with a probe with a molecular size similar to that of the reacting species, the higher EMF selectivity observed for the iron-containing samples can be related to the higher Lewis acid site concentration. In particular, B-Fe-BEA_200 exhibits a higher EMF selectivity than B-BEA due to the lower Brønsted acid site concentration, while the superiority of B-Fe-BEA_100 is due to the higher Lewis acid site concentration, despite its higher Brønsted acid site concentration. It is important to note that the iron-containing samples, i.e. B-Fe-BEA_100 and B-Fe-BEA_200, possesses very different Lewis-to-Brønsted acid site ratios, i.e. 1.2 and 1.7, respectively, while very similar EMF-to-EOP yield ratios are obtained. This results clearly indicate that a very small amount of iron is sufficient to favor EMF formation.

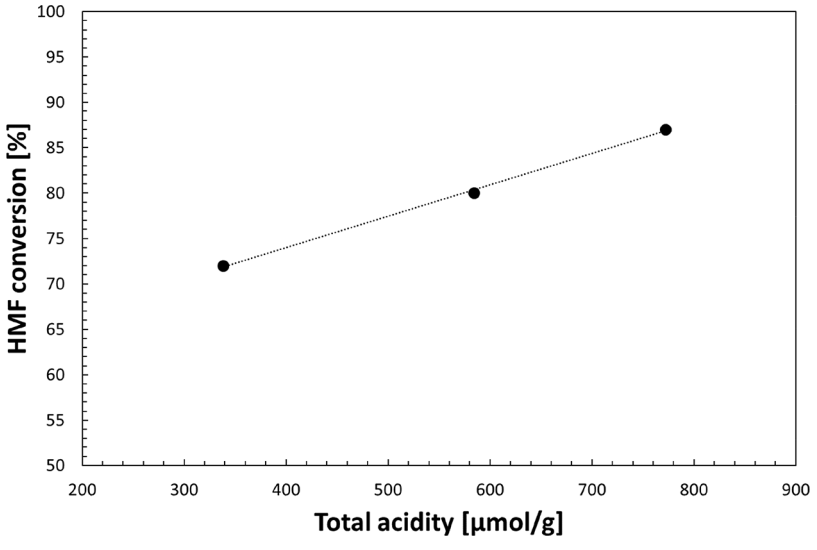

Figure 11. HMF conversion as a function of total acidity estimated by d_3-acetonitrile FTIR measurements.

https://doi.org/10.1021/acs.cgd.3c00085
Cryst. Growth Des. 2023, 23, 2988−3001

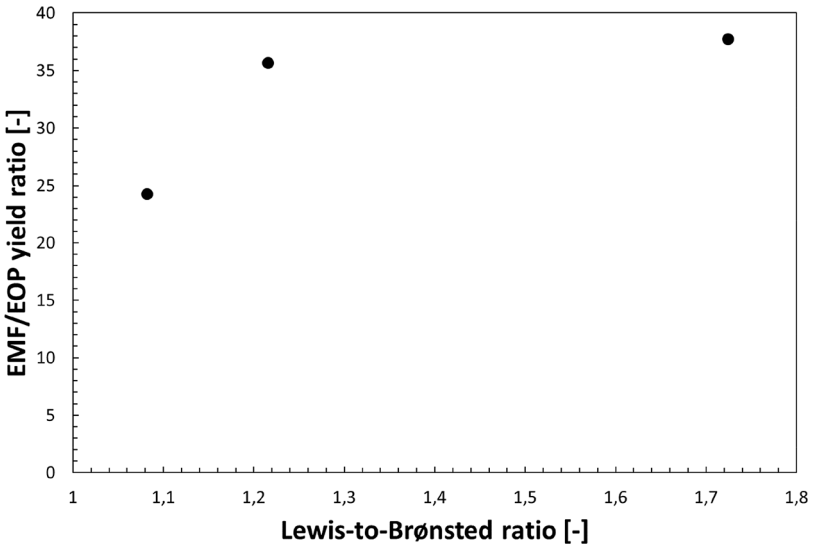

Figure 12. EMF-to-EOP yield ratio as a function of Lewis-to-Brønsted acid site ratio estimated by pyridine FTIR measurements.

4. CONCLUSION

In this work, high-silica Al-free BEA zeolite samples containing both boron and iron as trivalent atoms (with different Si/Fe ratios: i.e., 100, 200, and ∞) were synthesized by a simple procedure with tetraethylammonium (TEA^+) as template. The crystallization was carried out under hydrothermal conditions and for a period similar to that for conventional Al-rich BEA zeolite: i.e., a maximum of 6 days.

The incorporation of boron and iron had an effect on both the crystallinity and TEA^+−zeolite interaction, as observed by XRD and TG/DTA measurements, respectively. The surface acidity was studied by both NH_3-TPD and FT-IR, the latter in the presence of d_3-acetonitrile or pyridine as a probe molecule. The results reveal that the obtained BEA materials exhibit a very low acidity, with differences in terms of both silanols and Brønsted/Lewis distribution. In particular, the pyridine uptake was higher than d_3-acetonitrile uptake, indicating that the latter is not able to titrate the weak acid sites of the investigated samples. In particular, a significant difference between pyridine and d_3-acetonitrile adsorption uptake is observed for the iron-free B-BEA sample, suggesting the absence of iron allows obtaining a sample with a very weak acidity.

The liquid-phase HMF etherification with ethanol was adopted as a probe reaction to assess the catalytic features of the obtained high-silica BEA zeolite, as the product distribution is strongly affected by acid site distribution. The obtained results confirm that materials with low acidity and a high Lewis-to-Brønsted ratio are suitable for EMF formation, inhibiting the formation of EOP, which is favored by Brønsted acid sites.

In conclusion, the synthesis of high-silica BEA zeolite is challenging, but by using boron it is possible to stabilize the framework and obtain crystalline materials with low and weak acidity, with intriguing catalytic aspects when iron is also incorporated.

AUTHOR INFORMATION

Corresponding Author

Enrico Catizzone − *CECaSP_LAb-University of Calabria, 87036 Rende, Cosenza, Italy;* orcid.org/0000-0002-3962-9493; Email: enrico.catizzone@unical.it

Authors

Alessia Marino − *CECaSP_LAb-University of Calabria, 87036 Rende, Cosenza, Italy*

Massimo Migliori − *CECaSP_LAb-University of Calabria, 87036 Rende, Cosenza, Italy;* orcid.org/0000-0001-7775-516X

Giorgia Ferrarelli − *Department of ChiBioFarAm, University of Messina, INSTM CASPE (Laboratory of Catalysis for Sustainable Production and Energy) and ERIC aisbl-Viale F, 98165 Messina, Italy*

Alfredo Aloise − *Department of Physical and Chemical Sciences, University of L'Aquila, 67100 L'Aquila, Italy*

Donatella Chillè − *Department of ChiBioFarAm, University of Messina, INSTM CASPE (Laboratory of Catalysis for Sustainable Production and Energy) and ERIC aisbl-Viale F, 98165 Messina, Italy*

Georgia Papanikolaou − *Department of ChiBioFarAm, University of Messina, INSTM CASPE (Laboratory of Catalysis for Sustainable Production and Energy) and ERIC aisbl-Viale F, 98165 Messina, Italy*

Paola Lanzafame − *Department of ChiBioFarAm, University of Messina, INSTM CASPE (Laboratory of Catalysis for Sustainable Production and Energy) and ERIC aisbl-Viale F, 98165 Messina, Italy*

Siglinda Perathoner − *Department of ChiBioFarAm, University of Messina, INSTM CASPE (Laboratory of Catalysis for Sustainable Production and Energy) and ERIC aisbl-Viale F, 98165 Messina, Italy;* orcid.org/0000-0001-8814-1972

Gabriele Centi − *Department of ChiBioFarAm, University of Messina, INSTM CASPE (Laboratory of Catalysis for Sustainable Production and Energy) and ERIC aisbl-Viale F, 98165 Messina, Italy;* orcid.org/0000-0001-5626-9840

Girolamo Giordano − *CECaSP_LAb-University of Calabria, 87036 Rende, Cosenza, Italy;* orcid.org/0000-0003-2293-718X

Complete contact information is available at: https://pubs.acs.org/10.1021/acs.cgd.3c00085

Notes

The authors declare no competing financial interest.

https://doi.org/10.1021/acs.cgd.3c00085
Cryst. Growth Des. 2023, 23, 2988−3001

DEDICATION

Dedicated to Prof. Svetlana Mintova on her 60th birthday in recognition of her long and inspiring work on zeolite science and technology.

REFERENCES

(1) Čejka, J.; Mintova, S. Perspectives of Micro/Mesoporous Composites in Catalysis. *Catal. Rev. - Sci. Eng.* **2007**, *49* (4), 457−509.
(2) Peng, P.; Gao, X. H.; Yan, Z. F.; Mintova, S. Diffusion and Catalyst Efficiency in Hierarchical Zeolite Catalysts. *Natl. Sci. Rev.* **2020**, *7* (11), 1726−1742.
(3) Corma, A. From Microporous to Mesoporous Molecular Sieve Materials and Their Use in Catalysis. *Chem. Rev.* **1997**, *97* (6), 2373−2419.
(4) Palčić, A.; Valtchev, V. Analysis and Control of Acid Sites in Zeolites. *Appl. Catal. A Gen.* **2020**, *606*, 117795.
(5) Čejka, J.; Millini, R.; Opanasenko, M.; Serrano, D. P.; Roth, W. J. Advances and Challenges in Zeolite Synthesis and Catalysis. *Catal. Today* **2020**, *345*, 2−13.
(6) Boronat, M.; Corma, A. What Is Measured When Measuring Acidity in Zeolites with Probe Molecules? *ACS Catal.* **2019**, *9* (2), 1539−1548.
(7) Grand, J.; Awala, H.; Mintova, S. Mechanism of Zeolites Crystal Growth: New Findings and Open Questions. *CrystEngComm* **2016**, *18* (5), 650−664.
(8) Mintova, S.; Gilson, J.-P.; Valtchev, V. Advances in Nanosized Zeolites. *Nanoscale* **2013**, *5* (15), 6693−6703.
(9) Mintova, S.; Jaber, M.; Valtchev, V. Nanosized Microporous Crystals: Emerging Applications. *Chem. Soc. Rev.* **2015**, *44* (20), 7207−7233.
(10) Pérez-Botella, E.; Valencia, S.; Rey, F. Zeolites in Adsorption Processes: State of the Art and Future Prospects. *Chem. Rev.* **2022**, *122*, 17647.
(11) Wadlinger, R. L.; Kerr, G. T.; Rosinski, E. J. Catalytic Composition of a Crystalline Zeolite, U.S. Patent 3308069, 1967.
(12) Martínez, C.; Corma, A. Inorganic Molecular Sieves: Preparation, Modification and Industrial Application in Catalytic Processes. *Coord. Chem. Rev.* **2011**, *255* (13−14), 1558−1580.
(13) Weckhuysen, B. M.; Yu, J. Recent Advances in Zeolite Chemistry and Catalysis. *Chem. Soc. Rev.* **2015**, *44* (20), 7022−7024.
(14) Corma, A.; Navarro, M. T.; Rey, F.; Rius, J.; Valencia, S. Pure Polymorph C of Zeolite Beta Synthesized by Using Framework Isomorphous Substitution as a Structure-Directing Mechanism. *Angew. Chemie - Int. Ed.* **2001**, *40* (12), 2277−2280.
(15) Diaz-Cabanas, M. J.; Corma, A.; Moliner, M.; Cantin, A.; Jorda, J. L.; Zhang, D.; Sun, J.; Jansson, K.; Hovmoller, S.; Zou, X. Synthesis and Structure of Polymorph B of Beta Zeolite. *Stud. Surf. Sci. Catal.* **2008**, *174*, 233−236.
(16) Mihailova, B.; Valtchev, V.; Mintova, S.; Faust, A.-C.; Petkov, N.; Bein, T. Interlayer Stacking Disorder in Zeolite Beta Family: A Raman Spectroscopic Study. *Phys. Chem. Chem. Phys.* **2005**, *7* (14), 2756−2763.
(17) Borade, R. B.; Clearfield, A. Preparation of Aluminum-Rich Beta Zeolite. *Microporous Mater.* **1996**, *5* (5), 289−297.
(18) Bjorgen, M.; Kolboe, S. The Conversion of Methanol to Hydrocarbons over Dealuminated Zeolite H-Beta. *Appl. Catal. A Gen.* **2002**, *225* (1−2), 285−290.
(19) Otomo, R.; Yokoi, T.; Kondo, J. N.; Tatsumi, T. Dealuminated Beta Zeolite as Effective Bifunctional Catalyst for Direct Transformation of Glucose to 5-Hydroxymethylfurfural. *Appl. Catal. A Gen.* **2014**, *470*, 318−326.
(20) Silaghi, M. C.; Chizallet, C.; Raybaud, P. Challenges on Molecular Aspects of Dealumination and Desilication of Zeolites. *Microporous Mesoporous Mater.* **2014**, *191*, 82−96.
(21) Wang, Y.; Otomo, R.; Tatsumi, T.; Yokoi, T. Dealumination of Organic Structure-Directing Agent (OSDA) Free Beta Zeolite for Enhancing Its Catalytic Performance in n-Hexane Cracking. *Microporous Mesoporous Mater.* **2016**, *220*, 275−281.
(22) González, M. D.; Cesteros, Y.; Salagre, P. Comparison of Dealumination of Zeolites Beta, Mordenite and ZSM-5 by Treatment with Acid under Microwave Irradiation. *Microporous Mesoporous Mater.* **2011**, *144* (1−3), 162−170.
(23) Bregolato, M.; Bolis, V.; Busco, C.; Ugliengo, P.; Bordiga, S.; Cavani, F.; Ballarini, N.; Maselli, L.; Passeri, S.; Rossetti, I.; Forni, L. Methylation of Phenol over High-Silica Beta Zeolite: Effect of Zeolite Acidity and Crystal Size on Catalyst Behaviour. *J. Catal.* **2007**, *245* (2), 285−300.
(24) Van der Waal, J. C.; Rigutto, M. S.; van Bekkum, H. Synthesis of All-Silica Zeolite Beta. *J. Chem. Soc. Chem. Commun.* **1994**, 1241−1242.
(25) Camblor, M. A.; Corma, A.; Valencia, S. Spontaneous Nucleation and Growth of Pure Silica Zeolite-β Free of Connectivity Defects. *Chem. Commun.* **1996**, No. 20, 2365−2366.
(26) Serrano, D. P.; Van Grieken, R.; Sánchez, P.; Sanz, R.; Rodríguez, L. Crystallization Mechanism of All-Silica Zeolite Beta in Fluoride Medium. *Microporous Mesoporous Mater.* **2001**, *46* (1), 35−46.
(27) Mintova, S.; Reinelt, M.; Senker, J.; Metzger, T. H.; Bein, T. Pure Silica BETA Colloidal Zeolite Assembled in Thin Films. *Chem. Commun.* **2003**, *3* (3), 326−327.
(28) Mintova, S.; Valtchev, V.; Onfroy, T.; Marichal, C.; Knözinger, H.; Bein, T. Variation of the Si/Al Ratio in Nanosized Zeolite Beta Crystals. *Microporous Mesoporous Mater.* **2006**, *90* (1-3), 237−245.
(29) Larlus, O.; Mintova, S.; Wilson, S. T.; Willis, R. R.; Abrevaya, H.; Bein, T. A Powerful Structure-Directing Agent for the Synthesis of Nanosized Al- and High-Silica Zeolite Beta in Alkaline Medium. *Microporous Mesoporous Mater.* **2011**, *142* (1), 17−25.
(30) Schoeman, B. J.; Babouchkina, E.; Mintova, S.; Valtchev, V. P.; Sterte, J. Synthesis of Discrete Colloidal Crystals of Zeolite Beta and Their Application in the Preparation of Thin Microporous Films. *J. Porous Mater.* **2001**, *8* (1), 13−22.
(31) Majano, G.; Mintova, S.; Ovsitser, O.; Mihailova, B.; Bein, T. Zeolite Beta Nanosized Assemblies. *Microporous Mesoporous Mater.* **2005**, *80* (1−3), 227−235.
(32) Aloise, A.; Catizzone, E.; Migliori, M.; B. Nagy, J.; Giordano, G. Catalytic Behavior in Propane Aromatization Using GA-MFI Catalyst. *Chin. J. Chem. Eng.* **2017**, *25* (12), 1863.
(33) Yabushita, M.; Kobayashi, H.; Neya, A.; Nakaya, M.; Maki, S.; Matsubara, M.; Kanie, K.; Muramatsu, A. Precise Control of Density and Strength of Acid Sites of MFI-Type Zeolite Nanoparticles: Via Simultaneous Isomorphous Substitution by Al and Fe. *CrystEngComm* **2020**, *22* (44), 7556−7564.
(34) Liu, M.; Jia, S.; Li, C.; Zhang, A.; Song, C.; Guo, X. Facile Preparation of Sn-β Zeolites by Post-Synthesis (Isomorphous Substitution) Method for Isomerization of Glucose to Fructose. *Cuihua Xuebao/Chin. J. Catal.* **2014**, *35* (5), 723−732.
(35) Brazovskaya, E. Y.; Golubeva, O. Y. Study of the Effect of Isomorphic Substitutions in the Framework of Zeolites with a Beta Structure on Their Porosity and Sorption Characteristics. *Glas. Phys. Chem.* **2017**, *43* (4), 357−362.
(36) Aiello, R.; Nagy, J. B.; Giordano, G.; Katovic, A.; Testa, F. Isomorphous Substitution in Zeolites. *Comptes Rendus Chim.* **2005**, *8* (3−4), 321−329.
(37) Taramasso, M.; Perego, G.; B, N. Molecular Sieve Borosilicates. In *Proceedings of the fifth International Conference on Zeolite*; Rees, L. V. C., Ed.; Heyden: 1980; pp 40−48.
(38) Kallus, S.; Patarin, J.; Caullet, P.; Faust, A. C. Synthesis of Boron-Beta Zeolite from near-Neutral Fluoride-Containing Gels. *Microporous Mater.* **1997**, *10* (4−6), 181−188.
(39) de Ruiter, R.; Famine, K.; Kentgens, A. P. M.; Jansen, J. C.; van Bekkum, H. Synthesis of Molecular Sieve [B]-BEA and Modification of the Boron Site. *Zeolites* **1993**, *13* (8), 611−621.
(40) Pérez-Ramírez, J.; Groen, J. C.; Brückner, A.; Kumar, M. S.; Bentrup, U.; Debbagh, M. N.; Villaescusa, L. A. Evolution of Isomorphously Substituted Iron Zeolites during Activation: Comparison of Fe-Beta and Fe-ZSM-5. *J. Catal.* **2005**, *232* (2), 318−334.

https://doi.org/10.1021/acs.cgd.3c00085
Cryst. Growth Des. 2023, 23, 2988−3001

(41) Guzmán-Vergas, A.; Delahay, G.; Coq, B. Catalytic Decomposition of N2O and Catalytic Reduction of N2O and N2O + NO by NH3 in the Presence of O2 over Fe-Zeolite. *Appl. Catal. B Environ.* **2003**, *42* (4), 369−379.
(42) Mauvezin, M.; Delahay, G.; Kißlich, F.; Coq, B.; Kieger, S. Catalytic Reduction of N2O by NH3 in Presence of Oxygen Using Fe-Exchanged Zeolites. *Catal. Lett.* **1999**, *62* (1), 41−44.
(43) Centi, G.; Genovese, C.; Giordano, G.; Katovic, A.; Perathoner, S. Performance of Fe-BEA Catalysts for the Selective Hydroxylation of Benzene with N2O. *Catal. Today* **2004**, *91*−*92*, 17−26.
(44) Centi, G.; Perathoner, S.; Arrigo, R.; Giordano, G.; Katovic, A.; Pedulà, V. Characterization and Reactivity of Fe-[Al,B]MFI Catalysts for Benzene Hydroxylation with N2O. *Appl. Catal. A Gen.* **2006**, *307* (1), 30−41.
(45) Molino, A.; Migliori, M.; Macrì, D.; Valerio, V.; Villone, A.; Nanna, F.; Iovane, P.; Marino, T. Glucose Gasification in Super-Critical Water Conditions for Both Syngas Production and Green Chemicals with a Continuous Process. *Renew. Energy* **2016**, *91*, 451.
(46) Slak, J.; Pomeroy, B.; Kostyniuk, A.; Grilc, M.; Likozar, B. A Review of Bio-Refining Process Intensification in Catalytic Conversion Reactions, Separations and Purifications of Hydroxymethylfurfural (HMF) and Furfural. *Chem. Eng. J.* **2022**, *429*, 132325.
(47) Papanikolaou, G.; Lanzafame, P.; Giorgianni, G.; Abate, S.; Perathoner, S.; Centi, G. Highly Selective Bifunctional Ni Zeo-Type Catalysts for Hydroprocessing of Methyl Palmitate to Green Diesel. *Catal. Today* **2020**, *345*, 14.
(48) Papanikolaou, G.; Chillè, D.; Perathoner, S.; Centi, G.; Migliori, M.; Giordano, G.; Lanzafame, P. Use of Zeolites in Green Chemicals and Bio-Fuel Production via HMF Valorisation. *Microporous Mesoporous Mater.* **2022**, 112330.
(49) Lanzafame, P.; Papanikolaou, G.; Perathoner, S.; Centi, G.; Migliori, M.; Catizzone, E.; Aloise, A.; Giordano, G. Direct versus Acetalization Routes in the Reaction Network of Catalytic HMF Etherification. *Catal. Sci. Technol.* **2018**, *8* (5), 1304.
(50) Lanzafame, P.; Papanikolaou, G.; Perathoner, S.; Centi, G.; Migliori, M.; Catizzone, E.; Giordano, G. Reassembly mechanism in Fe-Silicalite during NH4OH post-treatment and relation with the acidity and catalytic reactivity. *Appl. Catal. A Gen.* **2019**, *580*, 186.
(51) Catizzone, E.; Aloise, A.; Migliori, M.; Giordano, G. Dimethyl Ether Synthesis via Methanol Dehydration: Effect of Zeolite Structure. *Appl. Catal. A Gen.* **2015**, *502*, 215−220.
(52) Milina, M.; Mitchell, S.; Michels, N. L.; Kenvin, J.; Pérez-Ramírez, J. Interdependence between Porosity, Acidity, and Catalytic Performance in Hierarchical ZSM-5 Zeolites Prepared by Post-Synthetic Modification. *J. Catal.* **2013**, *308* (1), 398−407.
(53) Barbera, K.; Bonino, F.; Bordiga, S.; Janssens, T. V. W.; Beato, P. Structure-Deactivation Relationship for ZSM-5 Catalysts Governed by Framework Defects. *J. Catal.* **2011**, *280* (2), 196−205.
(54) Miletto, I.; Catizzone, E.; Bonura, G.; Ivaldi, C.; Migliori, M.; Gianotti, E.; Marchese, L.; Frusteri, F.; Giordano, G. In Situ FT-IR Characterization of CuZnZr/Ferrierite Hybrid Catalysts for One-Pot CO2-to-DME Conversion. *Materials (Basel).* **2018**, *11* (11), 2275.
(55) Bourgeat-Lami, E.; Di Renzo, F.; Fajula, F.; Mutin, P. H.; Des Courieres, T. Mechanism of the Thermal Decomposition of Tetraethylammonium in Zeolite *β*. *J. Phys. Chem.* **1992**, *96* (9), 3807−3811.
(56) Perez-Pariente, J.; A. Martens, J.; A. Jacobs, P. Crystallization Mechanism of Zeolite Beta from (TEA)2O, Na2O and K2O Containing Aluminosilicate Gels. *Appl. Catal.* **1987**, *31* (1), 35−64.
(57) Derewinski, M.; Renzo, F. Di; Espiau, P.; Fajula, F.; Nicolle, M. A. Synthesis of Zeolite Beta in Boron-Aluminium Media. *Stud. Surf. Sci. Catal.* **1991**, *69* (C), 127−134.
(58) Niwa, M.; Katada, N. New Method for the Temperature-Programmed Desorption (TPD) of Ammonia Experiment for Characterization of Zeolite Acidity: A Review. *Chem. Rec.* **2013**, *13* (5), 432−455.
(59) Catizzone, E.; Migliori, M.; Mineva, T.; van Daele, S.; Valtchev, V.; Giordano, G. New Synthesis Routes and Catalytic Applications of Ferrierite Crystals. Part 1:1,8-Diaminooctane as a New OSDA. *Microporous Mesoporous Mater.* **2020**, *296*, 109987.
(60) Pieterse, J. A. Z.; Pirngruber, G. D.; van Bokhoven, J. A.; Booneveld, S. *Hydrothermal Stability of Fe-ZSM-5 and Fe-BEA Prepared by Wet Ion-Exchange for N2O Decomposition*; Elsevier: 2007; Vol. *170*. DOI: 10.1016/S0167-2991(07)81005-6.
(61) Armaroli, T.; Bevilacqua, M.; Trombetta, M.; Milella, F.; Alejandre, A. G.; Ramírez, J.; Notari, B.; Willey, R. J.; Busca, G. A Study of the External and Internal Sites of MFI-Type Zeolitic Materials through the FT-IR Investigation of the Adsorption of Nitriles. *Appl. Catal. A Gen.* **2001**, *216* (1−2), 59−71.
(62) Lanzafame, P.; Papanikolaou, G.; Perathoner, S.; Centi, G.; Giordano, G.; Migliori, M. Weakly Acidic Zeolites: A Review on Uses and Relationship between Nature of the Active Sites and Catalytic Behaviour. *Microporous Mesoporous Mater.* **2020**, *300*, 110157.
(63) Lanzafame, P.; Barbera, K.; Papanikolaou, G.; Perathoner, S.; Centi, G.; Migliori, M.; Catizzone, E.; Giordano, G. Comparison of H + and NH 4 + forms of zeolites as acid catalysts for HMF etherification. *Catal. Today* **2018**, *304*, 97.

https://doi.org/10.1021/acs.cgd.3c00085
Cryst. Growth Des. 2023, 23, 2988−3001